X-Ray Radiography Measurements of Diesel Spray Structure at Engine-Like Ambient Density

Alan L. Kastengren, Christopher F. Powell
Center for Transportation Research
Argonne National Laboratory
Argonne, IL 60439 USA

Yujie Wang, Kyoung-Su Im, and Jin Wang
Advanced Photon Source
Argonne National Laboratory
Argonne, IL 60439 USA

Abstract

X-ray radiography has been used to examine the dependence of the near-nozzle fuel distribution of diesel sprays on injection pressure and ambient density. Measurements of sprays from two nozzles with different geometries, one extensively hydroground and the other largely non-hydroground, have been obtained to show how nozzles of different geometries respond to changes in ambient density and rail pressure. The spray penetration near the nozzle demonstrates little dependence on ambient density but a strong dependence on rail pressure. Comparison of these results with standard correlations in the literature show that, in the near-nozzle region examined in this study, the penetration is expected to show little dependence on ambient density. The spray width becomes much larger for both nozzles as the ambient density increases. Rescaling the axial position by the square root of the density ratio between the fuel and the ambient gas accounts for the trends in spray width with ambient density for both nozzles. The radiography data can also be examined to determine the relative trends in the steady-state, mass-averaged axial velocity of the spray. The velocity decays more rapidly with axial distance as the ambient density increases. Rescaling the axial position also accounts for the trend of velocity decay with ambient pressure.

Introduction

Diesel sprays represent a complex and industrially-important flowfield. The structure of the spray has an important influence on the performance and emissions of diesel engines. Diesel spray flowfields are also particularly difficult to measure quantitatively. The flow contains numerous spray droplets, which obstruct the passage of visible light through the spray. The droplets can also scatter incoming light in multiple directions, confounding diagnostics which rely on scattered light.

As a result of these difficulties, a great deal of effort in diesel spray research has focused on the measurement of the penetration of the spray leading edge [1- 4] and the spray dispersion (cone angle) [1-3,5-7]. There is general acceptance in the literature that the spray penetration is characterized by a near-nozzle region where the spray penetration is linear with respect to time, followed by a far-field region where the spray penetration is proportional to the square root of time.

Studies of spray cone angle have shown that the density of the ambient gas has a strong effect on the cone angle. This relationship is usually represented as a power law dependence of the cone angle (or the tangent of the cone angle) on the density ratio between the injected fuel and the ambient gas. There is little agreement in the literature, however, regarding the value of the exponent of this power law relationship. Values of this exponent have ranged from 0.19 [1] to 0.5 [2,5].

Additional insights can be obtained by studies of variable-density gas jets. These jets differ significantly from diesel sprays; the density ratio between the jet fluid and the ambient fluid is much lower in variable-density gas jets than in sprays, and gas jets do not have the spray breakup and gas-droplet interaction phenomena seen in sprays. Nevertheless, variable-density gas jet flowfields are easier to measure than sprays, allowing for a more complete analysis of the flowfield. In variable-density jets, as in sprays, the width of the spray decreases as the ambient fluid becomes less dense relative to the jet fluid [8]. The jet concentration [9], ambient gas entrainment [10], and centerline velocity [11] trends with axial distance at different density ratio values can be collapsed onto a single curve by the use of an effective diameter. This diameter is given by:

$$d_{eff} = d_0 \sqrt{\frac{\rho_j}{\rho_a}} \qquad (1)$$

This effective diameter is the diameter of a jet of density ρ_a that would yield the same momentum at the same jet exit velocity as the jet with density ρ_j.

While the spray penetration and cone angle measurements delineate the extent of the spray, they provide little data regarding the internal fuel distribution of the spray. To overcome the limitations of optical diagnostics due to scattering in sprays, x-ray radiography has been developed as a spray diagnostic [12- 15]. X-rays are predominantly absorbed by spray droplets, rather than scattered, allowing quantitative measurements of spray structure to be made.

In the past, these measurements have largely focused on relatively low ambient density values (< 6 kg/m^3) [12-15]. While trends in the spray behavior with ambient density were examined in these studies, these ambient density values are far below those seen in operational diesel engines. In this study, these measurements will be extended to ambient density values of up to 34.0 kg/m^3. These values are much closer to those seen in operational diesel engines, significantly extending the applicability of these results.

Experimental Method

The x-ray radiography technique is based on a simple application of linear absorption. A monochromatic beam of x-rays passes through the spray, and the x-ray intensity passing through the spray is measured as a function of time. The x-ray intensity is first measured before the spray event. As the spray event occurs, fuel enters the path of the x-ray beam, absorbing part of the beam. This x-ray intensity can be converted into the fuel mass per unit area present in the beam with Eq. 2.

$$M(t) = \frac{\rho_\ell}{\varepsilon} \cdot \ln\left(\frac{I(t=0)}{I(t)}\right) \qquad (2)$$

Here $M(t)$ is the projected density at time t, ρ is the liquid density, ε is the absorption coefficient of the liquid (in mm^{-1}), I is the x-ray intensity at a particular time.

A monochromatic x-ray beam is needed to avoid the complicating factor of the x-ray wavelength dependence of the liquid x-ray absorption coefficient. In order to achieve sufficient monochromatic x-ray flux, a synchrotron light source is needed. The current experiments were performed at the 1-BM beamline at the Advanced Photon Source. The beamline uses a bending magnet synchrotron source and a series of x-ray optics to create a focused, monochromatic beam of x-rays. A pair of x-ray slits are used to define a narrow beam 160 μm in size full width, half maximum (FWHM) in the axial direction and 15 μm FWHM transverse to the injector axis. This beam passes through a pressurized spray chamber with x-ray transparent windows. After the beam passes

through the spray chamber, its intensity is measured using an avalanche photodiode (APD) detector. The time constant of the detector is less than 10 ns, allowing for time-accurate measurements of the x-ray intensity. The signal from the APD is recorded with a Yokogawa DL7480 500 MHz oscilloscope. The experimental setup is shown in Fig. 1.

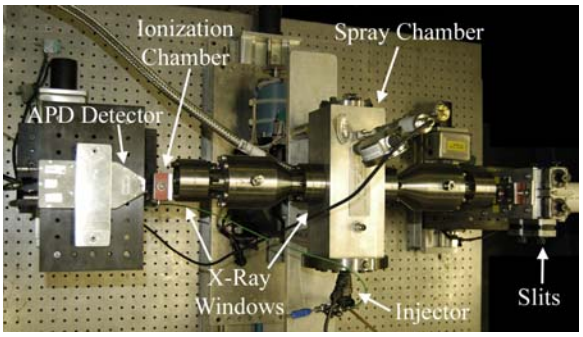

Figure 1. Experimental setup. The x-ray beam enters the setup from the right.

The x-ray beam from the Advanced Photon Source has a pulse structure. X-ray pulses occur every 155 ns in a pattern which repeats every 3.68 μs, corresponding to the fundamental cycle time of the synchrotron. The x-ray intensity for every x-ray pulse is determined, and the intensities are binned for every synchrotron cycle, yielding x-ray intensity data in arbitrary units every 3.68 μs. Using a time period before the spray event as the baseline intensity, Eq. 2 is applied to these data to obtain the projected density of the spray as a function of time. Further details regarding the data acquisition and analysis are given elsewhere [16].

While the radiography technique records the x-ray intensity as a function of time, the APD used in this experiment has no spatial resolution. The spatial resolution is determined by the x-ray beam size. To examine the spray structure in detail, the spray chamber is moved to various positions, allowing the data regarding spray density vs. time to be collected for many positions throughout the flowfield. Figure 2 shows an example of the measurement grids used in these experiments. Generally, data are obtained across the transverse extent of the spray wherever possible. The size of the x-ray windows limits the field of view in the axial direction and in the transverse direction near the end of the measurement domain. At every position in the flowfield, the x-ray intensity is recorded as an average of 32 spray events to improve the signal-to-noise ratio of the data. As such, these data show persistent, ensemble features of the spray flowfield, not shot-to-shot variability.

The radiography technique depends on strong absorption of the x-ray beam by the liquid fuel. This is especially important at high ambient density levels, since the ambient gas in the chamber can absorb a significant amount of the x-ray intensity. To increase the x-ray absorption coefficient of the fuel, a cerium fuel additive has been added in a 10% solution by volume. The properties of the fuel are listed in Table 1.

Table 1. Fuel physical properties

Density	873 kg/m3
Surface Tension	27.6 x 10-3 N/m
Kinematic Viscosity	3.65 cSt
X-ray Absorption Coefficient	2.53 x 10-3 m2/g

To study the effect of ambient density on spray behavior, the spray chamber was pressurized with N_2 at 5, 20, and 30 bar pressure. These experiments were performed at room temperature; thus, no vaporizing spray effects are present. While these ambient pressure values are much less than those seen in operational diesel engines near SOI, the ambient density values, particularly at 30 bar chamber pressure, approach those seen in operational diesel engines. Since the ambient density is accepted to have a much larger role in determining spray behavior than ambient pressure, these experiments give an appropriate representation of the non-evaporating spray structure.

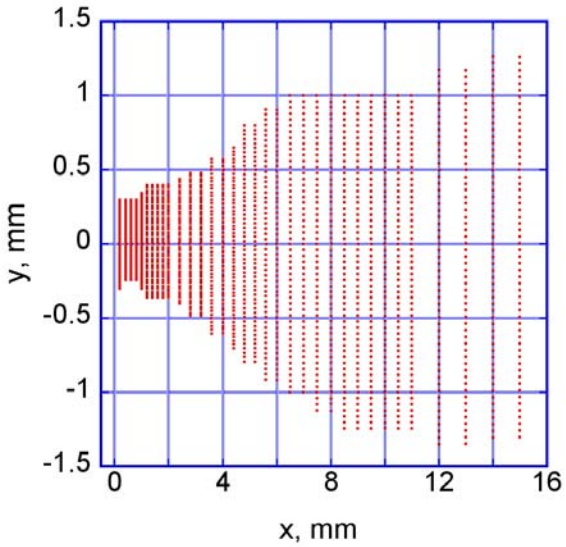

Figure 2. Measurement positions for the spray from the hydroground nozzle at 1000 bar rail pressure, 20 bar ambient pressure

The sprays in this study were produced with a Bosch common rail injection system using a light-

duty solenoid-based common rail diesel injector. Two axial single-hole injector tip geometries were examined. One nozzle was extensively hydroground, with an exit diameter of 183 µm. The other nozzle was not hydroground extensively and had a diameter of 207 µm. Both nozzles yield approximately the same steady-state flowrate.

Results

Example Images

Data were obtained at two levels of rail pressure (500 bar and 1000 bar), at three levels of ambient pressure (5 bar, 20 bar, and 30 bar), and with two nozzle geometries. Every possible combination of these parameters was measured, yielding 12 unique spray conditions. In the interests of brevity, only selected images from these measurements will be given.

Figure 3 shows an example of a spray shortly after the apparent SOI for the hydroground nozzle. Early in the injection event, the spray jet consists of a concentrated region near the injector with lower fuel concentrations as the jet moves downstream. The leading edge of the jet consists of a well-defined increase in projected density, allowing the leading edge to be tracked relatively easily.

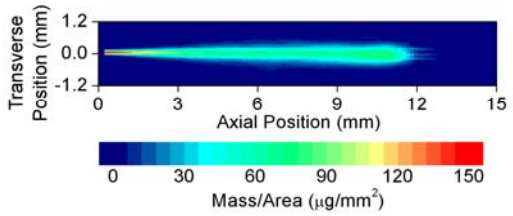

Figure 3. Spray projected density vs. position 72 µs after SOI for the hydroground nozzle, 1000 bar rail pressure, 20 bar ambient pressure

As has been described elsewhere [12], the spray from the hydroground nozzle is initially quite wide. This wide spray transitions after the injector fully opens into a narrow spray, which seems to represent the steady-state behavior of the spray. Figures 4-6 show the steady-state spray behavior for the hydroground nozzle at 5 bar, 20 bar, and 30 bar ambient pressure. As the data clearly show, as the ambient pressure, and hence ambient density, increases, the spray spreads much more rapidly as it proceeds downstream. These images were obtained at 1000 bar rail pressure; the behavior at 500 bar rail pressure is very similar.

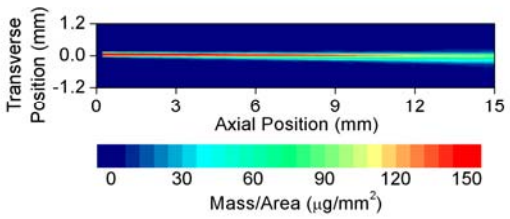

Figure 4. Spray projected density vs. position 750 µs after SOI for the hydroground nozzle, 1000 bar rail pressure, 5 bar ambient pressure

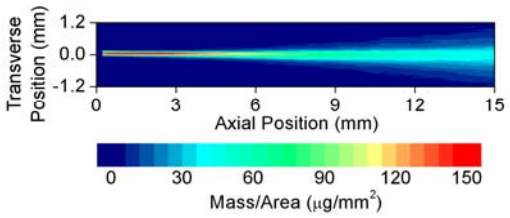

Figure 5. Spray projected density vs. position 750 µs after SOI for the hydroground nozzle, 1000 bar rail pressure, 20 bar ambient pressure

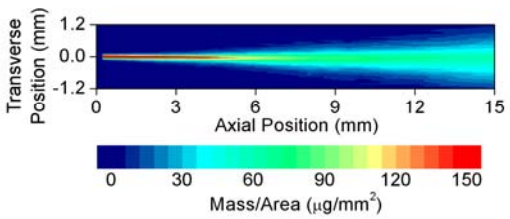

Figure 6. Spray projected density vs. position 750 µs after SOI for the hydroground nozzle, 1000 bar rail pressure, 30 bar ambient pressure

The spray distribution is significantly different for the non-hydroground nozzle, as shown in Figs. 7 and 8. Even at relatively low ambient density, the spray from the non-hydroground nozzle spreads much more quickly as it proceeds downstream than the spray from the hydroground nozzle. There is also a notable asymmetry in the spray. The spray is targeted preferentially downward in these images, with a relatively broad, low density region of fuel above the main concentration of fuel mass. The trend of steady-state spray behavior with ambient pressure, however, is similar to that seen for the hydroground nozzle. As the ambient pressure increases, the spray spreads much more quickly with downstream distance.

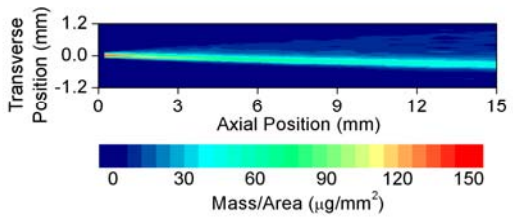

Figure 7. Spray projected density vs. position 750 μs after SOI for the non-hydroground nozzle, 500 bar rail pressure, 5 bar ambient pressure

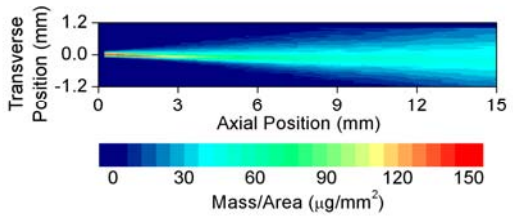

Figure 8. Spray projected density vs. position 750 μs after SOI for the non-hydroground nozzle, 500 bar rail pressure, 30 bar ambient pressure

Leading Edge Penetration

One of the most commonly studied properties of diesel sprays is the speed at which the leading edge of the spray propagates into the ambient gas. Previous studies [1-3] have developed correlations that have shown that the penetration speed is constant near the nozzle. Far from the nozzle, the penetration scales with $t^{1/2}$.

Figure 9 shows the penetration vs. time curves for the hydroground nozzle, while Fig. 10 shows the penetration vs. time for the non-hydroground nozzle. One of the most striking trends is that the ambient density has little effect on the spray penetration. With the exception of the spray from the non-hydroground nozzle at 500 bar rail pressure and 5 bar ambient pressure, the data at various ambient pressure values but the same rail pressure and nozzle geometry are quite similar. Higher rail pressure values lead to increased penetration speed, as expected from standard correlations. The differences between the nozzle geometries are fairly minor.

These data appear significantly different than typical penetration data, which show a negative curvature, rather than the positive curvature shown in the current data. The current data are, however, consistent with the literature. Previous studies [1,6] have shown that for a time period of tens of microseconds after the start of injection, the spray penetration has a positive curvature. The authors believe that this curvature is caused by the finite time required for the injector to open. Figure 9 shows the rate of injection for the hydroground with 1000 bar rail pressure, with a back pressure of approximately 20 bar. The rate of injection rapidly increases for the first approximately 50 μs before reaching a more or less steady-state value. It is logical that, in the first 50 μs of the spray event, as the injector opens and the rate of injection increases, the penetration speed would accelerate.

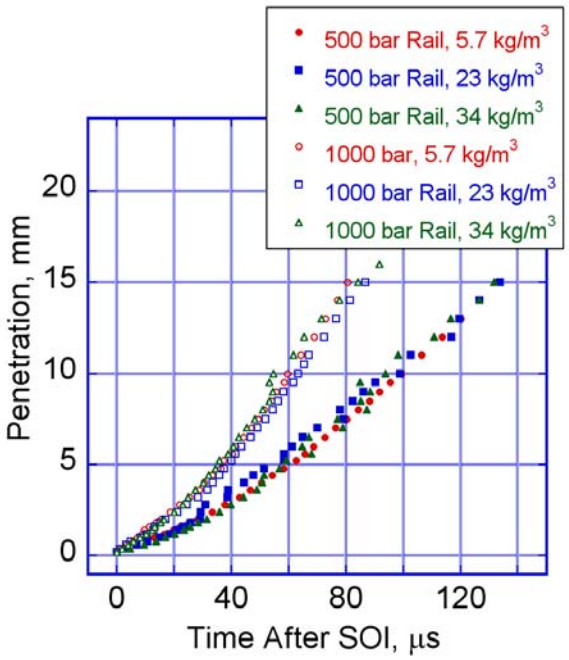

Figure 9. Spray penetration vs. time for the hydroground nozzle

One of the best-known penetration correlations has been given by Naber and Siebers [1]. In their work, they defined a characteristic length, x^+, that marked the transition between the penetration proceeding linearly with time vs. penetration proceeding proportionally with $t^{1/2}$. This distance indicates the distance at which interactions with the ambient gas become significant. The equation for x^+ is [1]:

$$x^+ = \frac{d_f}{a \cdot \tan(\theta/2)} \sqrt{\frac{\rho_\ell}{\rho_a}} \qquad (3)$$

To compare these data to the standard correlations of diesel spray penetration, Table 2 gives the characteristic length, as defined in Ref. 1, for the spray cases in this study. To calculate these lengths, the cone angle correlation given in Ref. 1 is used to calculate the optical cone angle, and the effective nozzle diameter is assumed to be 180 μm (slightly lower than the diameter of the hydroground nozzle). As shown in the table, most of the data shown in Figs. 9 and 10 are upstream of the characteristic

length. Thus, one would expect most of the data to show a linear trend of penetration with time. If one ignores the first 50 μs of the data record, when in the injector is opening, the penetration curves are indeed reasonably linear. One would expect that at 30 bar ambient pressure, one would begin to see a decrease in the slope of the penetration curve near the end of the curve, since the penetration is significantly greater than the characteristic length. Indeed, though it is difficult to detect in Figs. 9 and 10, the penetration begins to decelerate for $x > 10$ mm at 30 bar ambient pressure for both nozzles.

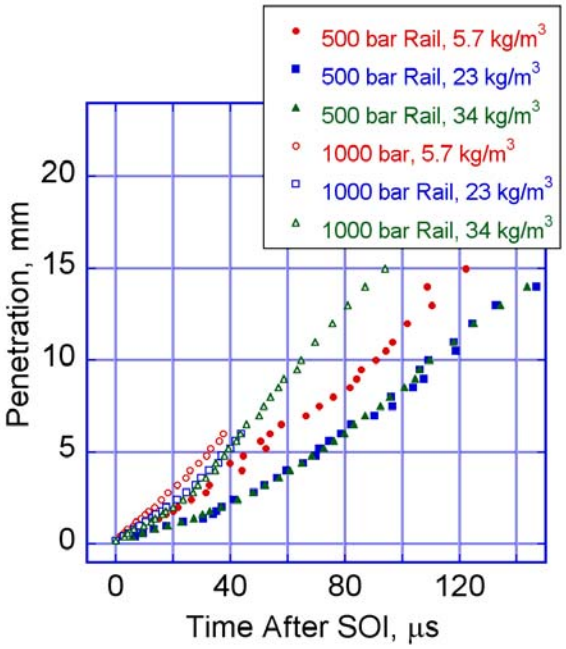

Figure 10. Spray penetration vs. time for the non-hydroground nozzle

Spray Cone Angle

As shown in Figs. 3-6, radiography shows the mass distribution of the spray as a function of time. This distribution can be used to determine the speading rate (cone angle) of the spray as a function of time. Unlike optical cone angle measurements, which focus on the spray periphery, cone angle measurements from radiography can be based on the behavior of the dense core of the spray, which contains most of the spray mass.

The first step in determining the spray cone angle is to define a width of the spray at several axial locations. In this study, the full-width, half maximum (FWHM) of the mass distributions across the spray are used. Though this definition of width is somewhat arbitrary, it is easily computed and contains much of the spray mass. If the underlying three-dimensional fuel distribution at an x position were Gaussian, the FWHM would contain ½ of the spray mass. The FWHM is determined for every time step in the measurement and for every axial location at which a significant amount of mass is located.

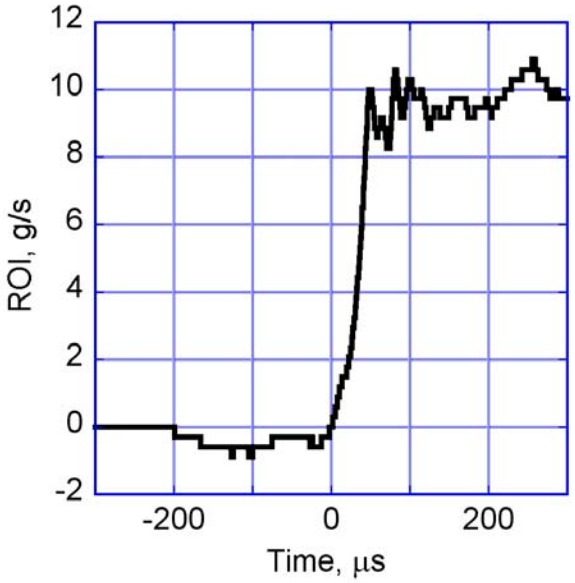

Figure 11. Initial rate of injection vs. time for the hydroground nozzle, 1000 bar rail pressure, and approximately 20 bar back pressure. Note that the time scale is arbitrary and not correlated precisely to the time scale in the x-ray data.

Table 2. Optical cone angle and characteristic length for penetration according to the correlations from Ref. 1

P_a bar	ρ_a kg/m^3	Cone Angle degrees	x+ mm
5	5.65	13.6	28.42
20	22.61	17.6	10.92
30	33.91	19.0	8.25

The trends of FWHM with respect to axial location are shown in Fig. 12 for the hydroground nozzle and Fig. 13 for the non-hydroground nozzle. These data were obtained 600 μs after SOI and have been averaged over 40 μs to improve the smoothness of the curves. These data show the steady-state behavior of the spray. The FWHM does not show a monotonic increase as the spray progresses downstream. The FWHM initially decreases slightly. The authors attribute this decrease to an evolution of the fuel distribution. Near the nozzle exit, the projected density distribution in a cross-section transverse to the nozzle axis has steeper sides and a flatter top than the distri-

butions farther downstream [12]. As such, more of the spray mass is contained within the FWHM near the nozzle exit than further downstream. As the tails of the mass distribution across the spray broaden and the peak of the distribution becomes sharper, the FWHM indeed decreases for a short distance. As one moves farther downstream, the shape of the projected density distribution becomes more stable, with the distributions becoming wider as the spray progesses downstream. The rate at which the mass distributions become wider as one moves downstream increases as the ambient pressure (and hence density) increases.

Given the results shown in Figs. 12 and 13, one could perform a linear fit to the FWHM vs. x data, excluding that near the nozzle, and derive a cone angle. Greater insight can be gained, however, by closer examination of the figure. The minimum value of FWHM, while similar for all three ambient pressure values, is reached progressively nearer the nozzle as the ambient pressure increases. This suggests that a rescaling of the *x*-coordinate may be necessary. As suggested by the literature regarding turbulent, variable density gas jets, the *x* coordinate is rescaled as:

$$x^* = \frac{x}{d_0}\sqrt{\frac{\rho_a}{\rho_\ell}} \qquad (4)$$

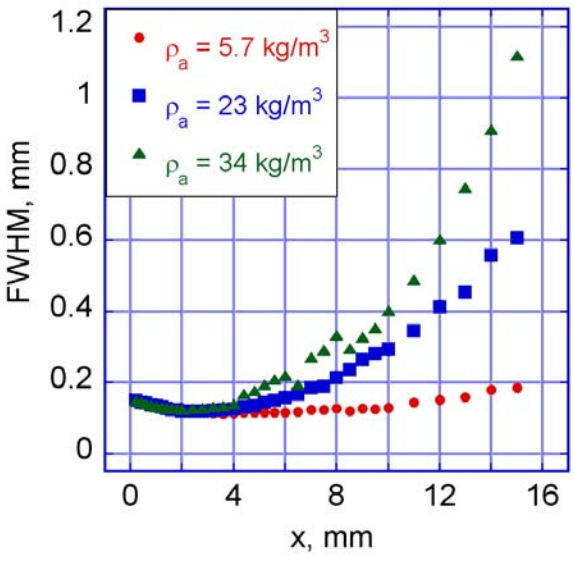

Figure 12. Trend in FWHM vs. x for various ambient pressure values for the hydroground nozzle 600-640 μs after SOI; rail pressure = 500 bar

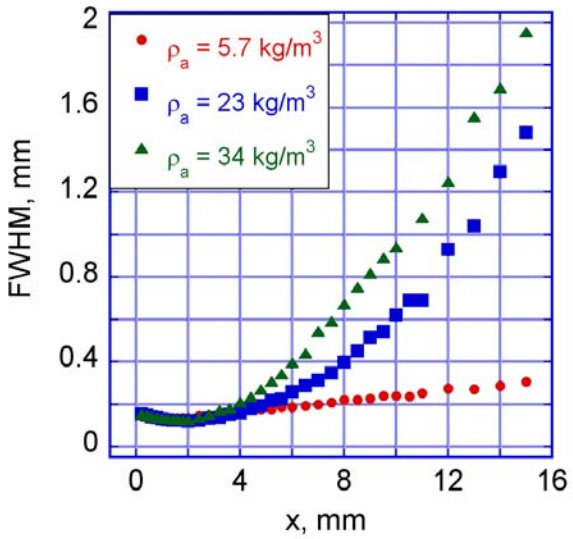

Figure 13. Trend in FWHM vs. x for various ambient pressure values for the non-hydroground nozzle 600-640 μs after SOI; rail pressure = 500 bar

Figure 14 shows the effect of rescaling the *x*-coordinate. A remarkable degree of similarity is seen between the curves at different ambient density values. Even at 1000 bar rail pressure, the agreement between the different datasets is remarkably good, as shown in Fig. 15.

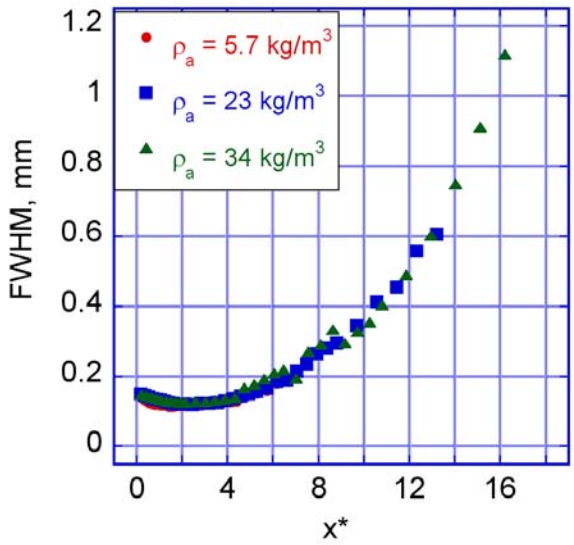

Figure 14. Trend in FWHM vs. normalized axial distance at various ambient pressure values for the hydroground nozzle 600-640 μs after SOI; rail pressure = 500 bar

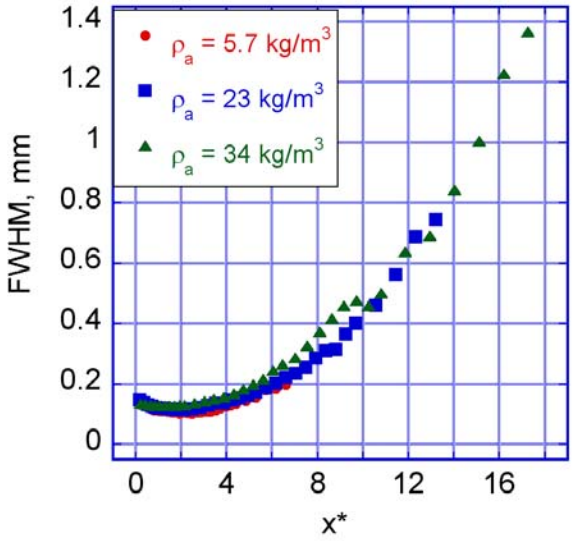

Figure 15. Trend in FWHM vs. normalized axial distance at various ambient pressure values for the hydroground nozzle 600-640 μs after SOI; rail pressure = 1000 bar

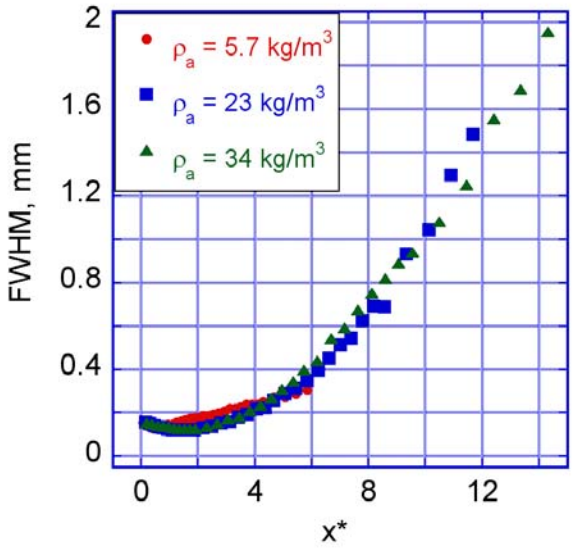

Figure 16. Trend in FWHM vs. normalized axial distance at various ambient pressure values for the non-hydroground nozzle 600-640 μs after SOI; rail pressure = 500 bar

This analysis can also be performed on the sprays from the non-hydroground nozzle. The data with x normalized according to Eq. 4 are shown in Fig. 16, which can be compared to the raw data in Fig. 13. Though the collapse of these data are not as striking as that seen in Figs. 14 and 15, particularly for the 5 bar ambient pressure case, this collapse still provides a significant simplification in understanding the trends in the raw data with ambient pressure.

This normalization also allows for interesting comparisons in the development of the sprays from the different nozzle geometries. For example, while the FWHM values near the nozzle are quite similar for both nozzle geometries, the FWHM increases significantly more quickly with axial distance for the non-hydroground nozzle. (Note the different vertical scales of Figs. 14 and 15 vs. Fig. 16.) This matches the qualitative behavior seen in the example images (Figs. 3-8). The trend of FWHM vs. x^* appears to be quite linear downstream of $x^* = 6$ for the non-hydroground nozzle (see Fig. 16). In contrast, for the hydroground nozzle, curvature is evident in Figs. 14 and 15 from the nozzle to at least x* = 10. These trends illustrate the well-known fact that internal nozzle geometry can strongly influence the development of diesel sprays.

Steady-State Spray Velocity

In addition to discussion of the spray penetration and cone angle, the fuel distribution data provided by x-ray radiography can also be used to examine the velocity of the spray. In previous work, it was demonstrated that radiography data could be used to determine the mass-averaged axial velocity as a function of x and time during the first stages of the injection event [17]. The mass-averaged axial velocity at any axial position was determined by:

$$V_{ma}(x_0,t) = \frac{\dot{m}_{cv}(x > x_0, t)}{TIM(x_0,t)} \qquad (5)$$

where V_{ma} is the mass-averaged axial velocity, TIM is the transverse integrated mass (an integral of the projected density across the spray), and $\dot{m}_{cv}$ is the mass flow through $x = x_0$. A major limitation of the previous work was the determination of the mass flow. This determination led to most of the uncertainty in the velocity determination and limited the analysis to the earliest stages of the injection event.

A method to avoid these difficulties is to consider the steady-state portion of the spray event. In order for the jet to be at steady-state, there can be no mass accumulation in any part of the spray domain. Thus, $\dot{m}_{cv}$ is no longer a function of x. By this analysis, during the steady-state portion of the spray event:

$$V_{ma}(x_0,t) \propto \frac{1}{TIM(x_0,t)} \qquad (6)$$

Thus, for any time step, the relative distribution of mass-averaged velocity as a function of x can be determined. While these values are only relative to each other, they can be used to examine how rapidly the axial velocity of the fuel decays as the spray progresses downstream.

Figures 17 and 18 show the evolution of the mass-averaged axial velocity 750 μs after SOI for the hydroground and non-hydroground nozzles, respectively, at 500 bar rail pressure. The data have been normalized by the mass-averaged axial velocity at the nozzle exit. It is clear that the ambient pressure (and therefore density) has a profound influence on the rate at which the fuel velocity decreases as the spray moves downstream. Nozzle geometry also has an effect, with a greater rate of decay in the velocity near the nozzle for the non-hydroground nozzle. The data at 1000 bar rail pressure are similar to those at 500 bar rail pressure.

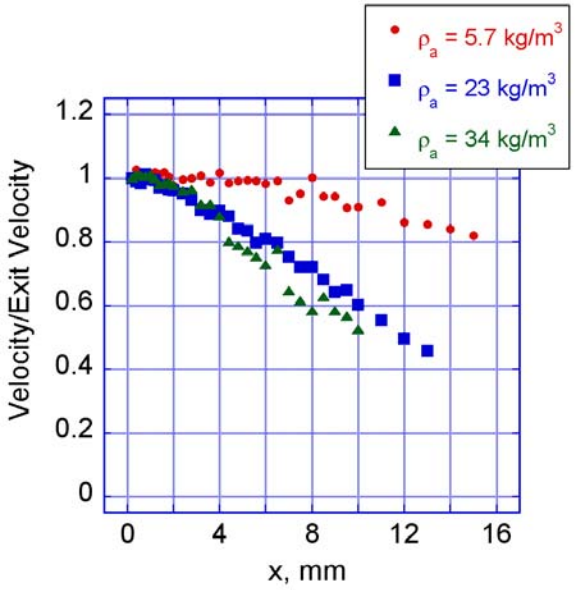

Figure 17. Trends in mass-averaged axial velocity vs. x for three ambient pressure values for the hydroground nozzle at 500 bar rail pressure

Given the success with which rescaling the data with an effective axial coordinate accounted for the trends in spray width with ambient density, it is natural to attempt such an analysis on these velocity data. Figures 19 and 20 show the velocity data shown in Figs. 17 and 18, respectively, but now plotted vs. x* rather than vs. x. It is clear from the figures that this rescaling largely collapses the mass-averaged axial velocity data from each nozzle onto a single curve. The rescaling is imperfect, however. Especially for the non-hydroground nozzle, there are still slight differences between the data at different ambient density values. On the whole, however, this rescaling serves to account for a large fraction of the trend in velocity decay with ambient density.

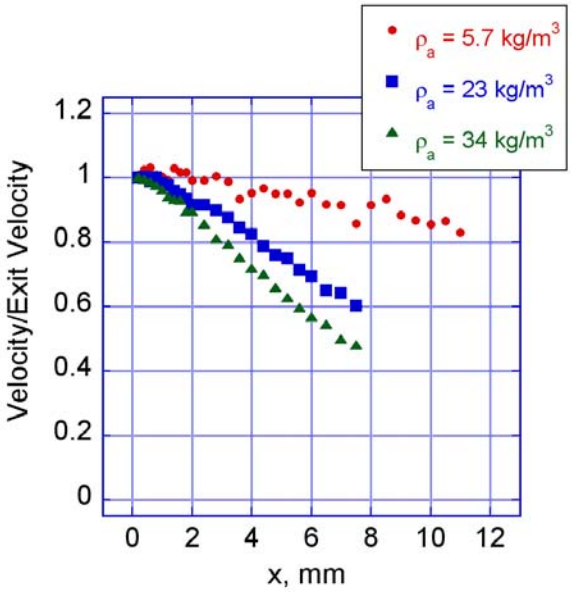

Figure 18. Trends in mass-averaged axial velocity vs. x for three ambient pressure values for the non-hydroground nozzle at 500 bar rail pressure

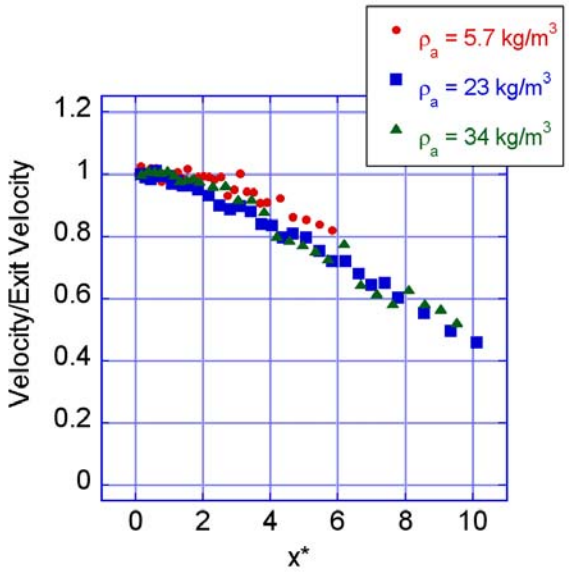

Figure 19. Trends in mass-averaged axial velocity vs. x* for three ambient pressure values for the hydroground nozzle at 500 bar rail pressure

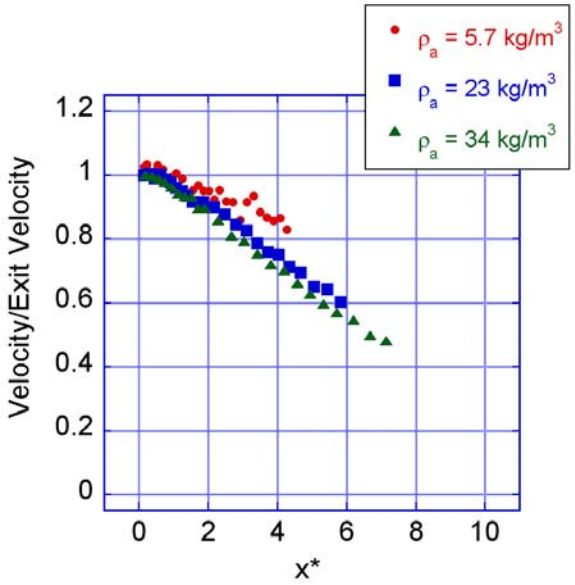

Figure 20. Trends in mass-averaged axial velocity vs. x* for three ambient pressure values for the non-hydroground nozzle at 500 bar rail pressure

Discussion

As mentioned previously, the literature on variable-density turbulent gas jets strongly suggests that, to understand the dynamics of the jet, the axial coordinate should be rescaled by the square root of the density ratio between the jet and ambient fluid. In terms of both the spray width and the decay in the mass-averaged axial velocity at steady state, it appears that this scaling is also effective for the near-nozzle region of the diesel sprays studied in this work. This result also supports the conclusion by some works in the diesel spray literature that the spray cone angle is proportional to $(\rho_a/\rho_\ell)^{1/2}$ [2,5].

In the study of turbulent jets, it is generally accepted that the flow is not fully developed until 30-40 effective nozzle diameters downstream of the nozzle [18]. This helps to explain the curvature of the plots of spray width vs. x*. Even at the most downstream x^* locations, the jet is not yet fully developed. Thus, it should not be surprising that the linear dependence of spray width on x^* seen in fully-developed turbulent jets is not entirely evident in these data.

It is interesting to compare the scaling used in this study (x^*) with the characteristic length used in the penetration correlation in Ref. 1. If this characteristic length is normalized using Eq. 4, it becomes:

$$\left(x^+\right)^* = \frac{1}{0.66 \cdot \tan(\theta/2)} = \frac{1.5}{\tan(\theta/2)} \quad (7)$$

For values of the optical cone angle from 10-20°, this yields an x^* value at the characteristic length of 8.5 to 17. Thus, it seems that for typical values of the spray width, this characteristic length lies well within the developing region of the spray. It is indeed of the same order of magnitude as the potential core length seen in variable-density turbulent jets [11].

The development of the jet also has implications in applied diesel jets. In high-speed, small-bore diesel engines, the distance which the jet can penetrate before it impinges on the piston bowl is in the range of 30-50 mm. In this case, at ambient density values of roughly 30 kg/m^3, the interactions of the jet with the piston bowl (main injection events) or cylinder wall (pre- or post-injection events) may begin before the jet becomes truly fully developed. In this case, there is no fully-developed jet region in the spray, even if the effects of combustion and evaporation on the jet are ignored.

It is also striking how quickly the spray velocity decays with axial distance. Within x* = 10 of the nozzle, the mass-averaged axial spray velocity is ½ or less of the injection velocity, even in the spray from the hydroground nozzle, which is particularly narrow. This indicates that the exchange of momentum between the ambient gas and the fuel is quite strong.

Conclusions

The effect of ambient density on the structure of diesel sprays has been examined using x-ray radiography. Radiography allows the mass distribution in sprays to be examined in a quantitative fashion as a function of time. Sprays were examined at different ambient density values (5.66 kg/m^3, 22.6 kg/m^3, and 33.9 kg/m^3) and rail pressure values (500 and 1000 bar), as well as with two nozzle geometries (hydroground and non-hydroground). While rail pressure has a significant effect on the spray penetration near the nozzle, the ambient density has no significant effect. In accordance with penetration correlations from the literature, the spray region examined in this study is dominated by the injected fluid, rather than the ambient gas, so the lack of influence from the ambient density is not unexpected. Due to the nonlinear behavior of the spray width as a function of axial distance, it is problematic to define a cone angle from the radiography data. It is clear, however, that the non-hydroground nozzle yields a wider spray than the hydroground nozzle. The spray width data show that for both nozzles, rescaling the axial distance in the data with the square root of the density ratio between the fuel and the ambient gas can collapse the trends in spray width as the ambient density changes. Analysis of the steady-state mass-averaged axial velocity of the spray as a function of x also shows that rescaling the x coordinate largely collapses the data onto a single curve for each nozzle geometry.

Nomenclature

$FWHM$	=	Full-width, half maximum
I	=	X-ray intensity
M	=	Projected density of spray, μg/mm^2
P_a	=	Ambient pressure, bar
SOI	=	Apparent start of injection, defined as the time when the spray penetration reaches the first measurement position
TIM	=	Transverse integrated mass, kg/m
V_{ma}	=	Mass-averaged axial velocity, m/s
a	=	0.66; fitting constant from the penetration correlation of Ref. 1.
d_{eff}	=	Effective nozzle diameter, accounting for density ratio effects, m
d_f	=	Effective diameter of the nozzle, accounting for discharge coefficient effects, m
$\dot{m}_{cv}$	=	Mass flow through a particular x position, kg/s
x	=	Axial position, mm
x^*	=	Rescaled axial position, dimensionless
x^+	=	Characteristic length from the penetration correlation of Ref. 1, mm
y	=	Position transverse to the spray axis, mm
ε	=	Fuel absorption coefficient, mm^{-1}
θ	=	Spray cone angle, degrees
ρ_a	=	Ambient density, kg/m^3
ρ_j, ρ_ℓ	=	Density of the jet fluid (i.e., fuel), kg/m^3

Acknowledgements

The submitted manuscript has been created by UChicago Argonne, LLC, Operator of Argonne National Laboratory ("Argonne"). Argonne, a U.S. Department of Energy Office of Science laboratory, is operated under Contract No. DE-AC02-06CH11357. The U.S. Government retains for itself, and others acting on its behalf, a paid-up nonexclusive, irrevocable worldwide license in said article to reproduce, prepare derivative works, distribute copies to the public, and perform publicly and display publicly, by or on behalf of the Government. This research was performed at the 1-BM-C beamline of the Advanced Photon Source, Argonne National Laboratory. The authors acknowledge the support of this work from the Department of Energy Vehicle Technologies Program.

References

[1] Naber, J. and Siebers, D., 1996, "Effects of Gas Density and Vaporization on Penetration and Dispersion of Diesel Sprays," SAE Paper 960034.

[2] Araneo, L., Coghe, A., Brunello, G., and Cossali, G. E., 1999, "Experimental Investigation of Gas Density Effects on Diesel Spray Penetration and Entrainment," SAE Paper 1999-01-0525.

[3] Hiroyasu, H. and Arai, M., 1990, "Structures of Fuel Sprays in Diesel Engines," SAE Paper 900475.

[4] Desantes, J., Payri, R., Salvador, F., and Soare, V., 2005, "Strudy of the Influence of Geometrical and Injection Parameters on Diesel Sprays Characteristics in Isothermal Conditions," SAE Paper 2005-01-0913.

[5] Wu. K.-J., Su, C.-C., Steinberger, R., Santavicca, D., and Bracco, F., "Measurements of the Spray Angle of Atomizing Jets," *Journal of Fluids Engineering*, v. 105, December 1983, pp. 406-413.

[6] Heimgärtner, C. and Liepertz, A., 2000, "Investigation of the Primary Spray Breakup Close to the Nozzle of a Common-Rail High Pressure Diesel Injection System," SAE Paper 2000-01-1799.

[7] Verhoeven, D., Vanhemelryck, J.-L., and Baritaud, T., 1998, "Macroscopic and Ignition Characteristics of High-Pressure Sprays of Single-Component Fuels," SAE Paper 981069.

[8] Elzawawy, A., Bravo, L., Andreopoulos, Y., and Watkins, C., 2007, "Compressibility and Density Effects in Free Subsonic Jet Flows: Three Dimensional PIV Measurements of Turbulence," AIAA Paper 2007-2858.

[9] Pitts, W., 1991, "Effect of global density ratio on the centerline mixing behavior of axisymmetric turbulent jets," *Experiments in Fluids*, v. 11, pp. 125-134.

[10] Ricou, F. and Spalding, D., 1963, "Measurement of entrainment by axisymmetrical turbulent jets," *Journal of Fluid Mechanics*, v. 11, pp. 21-32.

[11] Sautet, J. and Stepowski, D., 1995, "Dynamic behavior of variable-density, turbulent jets in their near development fields," *Physics of Fluids*, v. 7, n. 11, November 1995, pp. 2796-2806.

[12] Kastengren, A., Powell, C.F., Riedel, T., Cheong, S.-K., Im, K.-S., Liu, X., Wang, Y.-J., and Wang, J. "Nozzle Geometry and Injection Duration Effects on Diesel Sprays Measured by X-Ray Radiography," in press, *Journal of Fluids Engineering.*

[13] Cheong, S.-K., Liu, J., Shu, D., Wang, J., and Powell, C.F., 2004, "Effects of Ambient Pressure on Dynamics of Near-Nozzle Diesel Sprays Studied by Ultrafast X-Radiography," SAE Paper 2004-01-2026.

[14] Powell, C.F., Ciatti, S., Cheong, S.-K., Liu, J., and Wang, J., 2004, "X-Ray Absorption Measurement of Diesel Sprays and the Effect of Nozzle Geometry," SAE Paper 2004-01-2011.

[15] Kastengren, A., Powell, C.F., Wang, Y.-J., and Wang, J., "Study of Diesel Jet Variability Using X-Ray Radiography," in press, *Journal of Engineering for Gas Turbines and Power.*

[16] Kastengren, A. and Powell, C.F., 2007, "Spray Density Measurements Using X-Ray Radiography," *Proceedings of IMechE Part D: Journal of Automobile Engineering*, v. 221, n. 6, pp. 653-662.

[17] Kastengren, A., Powell, C.F., Riedel, T., Cheong, S.-K., Im, K.-S., Liu, X., Wang, Y.-J., and Wang, J., 2007, "Determination of Diesel Spray Axial Velocity Using X-Ray Radiography," SAE Paper 2007-0666.

[18] Pope, S., 2000, *Turbulent Flows*, Cambridge University Press, Cambridge, pp. 97-99.